

Scattering Model for Grazing Impact of Micro-Particles on Mirror Surfaces

E. Farahvashi⁽¹⁾, K. D. Bunte⁽²⁾, M. Traud⁽³⁾, M. Millinger⁽⁴⁾, Y. Li⁽⁵⁾, R. Srama⁽⁶⁾

⁽¹⁾ *etamax space GmbH, Lilienthalplatz 1, 38108 Braunschweig, Germany, Email: e.farahvashi@etamax.de*

⁽²⁾ *etamax space GmbH, Lilienthalplatz 1, 38108 Braunschweig, Germany, Email: k.bunte@etamax.de*

⁽³⁾ *etamax space GmbH, Lilienthalplatz 1, 38108 Braunschweig, Germany, Email: m.traud@etamax.de*

⁽⁴⁾ *European Space Agency/ESTEC, Keplerlaan 1, 2201 AZ Noordwijk, Netherlands, Email: mark.millinger@esa.int*

⁽⁵⁾ *Institut für Raumfahrtssysteme, Universität Stuttgart, Pfaffenwaldring 29, 70569 Stuttgart, Germany, Email: li@irs.uni-stuttgart.de*

⁽⁶⁾ *Institut für Raumfahrtssysteme, Universität Stuttgart, Pfaffenwaldring 29, 70569 Stuttgart, Baylor University, Waco, TX, USA, Email: srama@irs.uni-stuttgart.de*

ABSTRACT

Micro-meteoroids can pose a risk to X-ray optics since the particles can enter the nested mirror system at shallow angles resulting in a focused cascading of fragments along the system towards the CCD camera, damaging the camera and the mirror surfaces along their path. Consequently, a statistical model was developed based on data from dedicated hypervelocity impact tests to characterize the fragmentation behaviour of projectiles impacting on a mirror surface at shallow angles. The predictions of the model were validated against the hypervelocity impact test data and a good compliance could be observed. Consequently, the model can be used to study the damage severity of the focused cascading effects inside X-ray optic instruments. A possible application example is provided.

1 INTRODUCTION

The environment around a spacecraft contains various solid particles distributed along a wide range of sizes, ranging from some meters (e.g. rocket bodies) to a few micrograms such as micro-meteoroids. Despite their small size, micro-particles can pose a threat to spacecraft surfaces and particularly to optical sensors as the particles can reach relative velocities of several tens of kilometres per second. One example of such sensors are Wolter telescopes which typically consist of many nested grazing incident mirrors to reflect the incoming X-rays at very shallow angles to focus them towards a common focal point. However, the analysis of the PN-CCD camera system aboard XMM-Newton indicates that the structure of the X-ray optics also leads to a focused cascading of micro-particles entering the mirror system at grazing impact angles [1]. In addition, the cascading along the mirror system may cause a degradation of the mirror surfaces. Thus, it reduces the efficiency of the telescope and damage the CCD camera.

Therefore, an urge arises to analyse the vulnerability of X-ray detectors due to micro-particle focussing based on

the mission environment and as such to determine the probability of instrument damage. However, currently, there is no model available to characterise the scattering of micro-particles at such grazing incident angles. The development of such a model and its implementation into micro-meteoroids and orbital space debris (MMOD) impact risk assessment tools such as ESABASE2/Debris would allow a detailed vulnerability assessment of X-ray optic instruments against micro-particles based on the instrument geometry and mission parameters (orbit, duration etc.)

As a result, a series of hypervelocity impact (HVI) tests with micro-particles were performed on single mirror plates at grazing angles to observe the characteristics of the projectile scattering. Based on the obtained test data, a statistical model was developed to simulate the scattering and cascading of particles impacting X-ray mirrors with grazing angles.

This paper describes the model development process including HVI data analysis, model implementation and model validation. Furthermore, the application feasibility of the model in ESA's ESABASE2/Debris tool is demonstrated. Hereby, the focus is solely put on the mathematical explanation of the model development and not on the explanation of the physical findings.

This study was performed under the ESA contract nr. 4000170405/17/NL/LF.

2 DATA ANALYSIS

2.1 Data Acquisition

In the framework of this study, several HVI tests were performed for two types of projectiles to simulate the different kind of micro-meteoroid material composition [2]. As typical material compositions for micro-meteoroids, Iron and Olivine particles were applied as representatives of ductile and brittle materials respectively.

As the focus of this paper lies on the model development,

the test setup is addressed briefly to highlight relevant factors for the test data acquisition. The simplified test setup is illustrated in Fig. 1. The particles stream first passes through a Beamline Detector in which the mass and velocity of the projectile are recorded. Afterwards, the particles are directed towards a rotatable mirror that can be inclined at specific angles towards the particle stream. The generated projectile fragments hit a Microchannel-Plate (MCP) where the mass and velocity of the fragments are determined. Lastly, the spatial 2D location of the fragments is determined via a Delayline Detector (DLD).

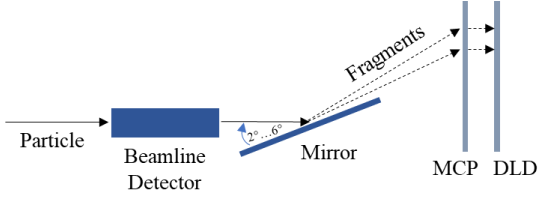


Figure 1. Hypervelocity impact test setup consisting of a Beamline Detector, a rotatable mirror, a Microchannel-Plate (MCP) and a Delayline Detector (DLD).

With the help of the adjustable mirror, the tests were performed for the three grazing impact angle categories: 2°, 4° and 6°. The velocity of the spherical particles ranges between 4-50 km/s with masses between 10^{-19} kg to 10^{-14} kg. Due to the test setup and measurement instruments, the calibration demonstrated an uncertainty of less than 2 mm for fragment location and an uncertainty of a factor about 10 for fragment mass.

2.2 Reference Coordinate System

The coordinate system for describing the projectile and fragment trajectory is defined in Fig. 2. The reference frame is impact oriented, meaning that the origin of the coordinate system is located at the impact location on the target surface while the X-axis follows the down-stream of the projectile direction. Hereby, The X-Y-Plane describes the target surface and the Z-axis follows the target surface normal. The elevation angle of projectile and fragment is measured from the X-Y-plane and the azimuth angle is measured from the X-axis. A clockwise rotation is considered as positive for all angles. Lastly, the following condition for projectile azimuth always applies: $\varphi_{proj} = 0^\circ$.

2.3 Data Content

The HVI tests generated 2370 datasets with each dataset representing a detected fragment. The content of a single fragment dataset is summarised in Tab. 1 while distinguishing between fragment parameters and the parameters of the projectile from which the fragment is originated.

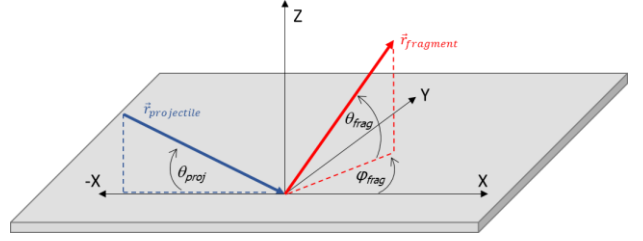


Figure 2. Model reference coordinate system with X-Y-plane describing the target surface, θ_{proj} being projectile elevation and θ_{frag} and φ_{frag} being fragment elevation and azimuth respectively.

Table 1. Content overview of a fragment dataset gained from hypervelocity impact tests.

Originating Projectile Parameters	Fragment Parameters
Projectile ID	Fragment ID
Mass	Mass
Velocity	Velocity
Elevation	Elevation
Density	Azimuth
Material Type (Olivine / Iron)	

3 MODEL DEVELOPMENT

3.1 Model Overview

The core functionality of the developed model “GRIM” (Grazing Impact Scattering Model) is based on a statistical approach, meaning that each fragment property is determined based on a probability density function (PDF) from which a value is generated via a random number generator. The advantage of this approach is that a pseudo-chaotic fragmentation behaviour is introduced to resemble the chaotic nature of the fragmentation process observed in the HVI test data. The PDFs are derived by analysing the dependencies of the fragment properties with the projectile properties as well as with other properties of the fragment itself.

Moreover, a parametric approach was introduced to consider the ductile and brittle projectile categories. The projectile type specific coefficients are used in the PDFs to predict the resulting fragment properties.

Applying the above approaches allows GRIM to use the projectile properties as input parameter to predict the resulting fragment properties.

3.2 Data Correlation

To define the model workflow and the PDFs, a correlation analysis was performed to determine the dependencies between fragment-to-projectile as well as fragment-to-fragment properties. For the correlation analysis as well as for the PDF definition, the following relative fragment parameters were introduced additionally to the dataset:

- $m_{frag}/m_{frag,tot}$: Ratio of fragment mass to the total fragment mass generated in the same impact event,
- $m_{frag,tot}/m_{proj}$: Ratio of total fragment mass detected in the impact event to the projectile mass,
- V_{frag}/V_{proj} : Ratio of fragment velocity to projectile velocity,
- $\theta_{frag}/\theta_{proj}$: Ratio of fragment elevation to projectile elevation,
- N_{frag} : Number of generated fragments per impact event,
- $E_{kin,imp}$: Kinetic energy of the projectile orthogonal to target surface (see Eq. 1).

$$E_{kin,imp} = \frac{m_{proj} \cdot [V_{proj} \cdot \sin(\theta_{proj})]^2}{2} \quad (1)$$

As indicated by Fig. 3, the following correlations were observed:

1. N_{frag} correlates with $E_{kin,imp}$: The higher the kinetic impact energy, the higher the quantity of generated fragments
2. Azimuth distribution of the fragments correlates with N_{frag} : The higher the fragment quantity per impact, the wider the azimuth spreading cone
3. $m_{frag}/m_{frag,tot}$ inversely correlates with N_{frag} : The higher the fragment quantity per impact, the lower the mean mass of the individual fragments compared to the total fragment mass
4. V_{frag}/V_{proj} correlates with $m_{frag}/m_{frag,tot}$: The higher the mass portion of a fragment compared to the total fragment mass, the more its velocity resembles the projectile velocity.
5. $\theta_{frag}/\theta_{proj}$ correlates inversely with θ_{proj} and with V_{frag}/V_{proj} : The lower the fragment velocity and the lower the projectile incident angle, the higher the relative fragment elevation.

3.3 Probability Density Functions

For each fragment property, a PDF was generated to express the distribution probability of the fragments detected in the HVI tests. The PDFs were defined based on the observed correlations. These PDFs are presented

in the following sections. For demonstrational purpose, the plots hereafter only cover the distribution of Iron projectiles.

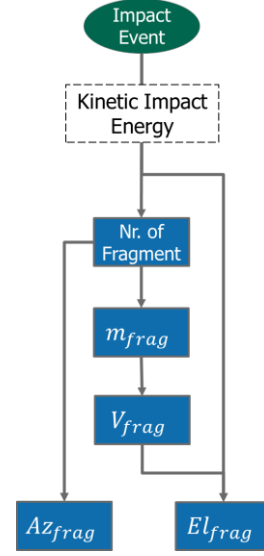


Figure 3. Fragment properties correlations.

3.3.1 Fragment Quantity Distribution

PDF

The distribution of the number of detected fragments per impact event N_{frag} is shown in Fig. 5 for different kinetic impact energy $E_{kin,imp}$ bins. Hereby, an exponential PDF as in Eq 2 has been selected for the distribution (red dotted line).

$$f(x, \lambda_{expon}) = \lambda_{expon} \cdot e^{-\lambda_{expon} \cdot (x-1)} \quad (2)$$

PDF Parameters

The resulting distribution of the log-exponential parameter λ_{expon} as a function of $E_{kin,imp}$ is shown in Fig.4. Additionally, a weighted logarithmic exponential regression (red dotted line) as in Eq. 3 is used to fit the distribution. The equation coefficients are listed in Tab. 2.

$$\lambda_{expon}(E_{kin,proj}) = a_n \cdot e^{-b_n \cdot \log(E_{kin,proj})} + c_n \quad (3)$$

Table 2. Coefficients for λ_{expon}

Parameter	a_n	b_n	c_n
Brittle (Olivine)	0.00038	0.3	0.03
Ductile (Iron)	1.1e-6	0.45	0.094

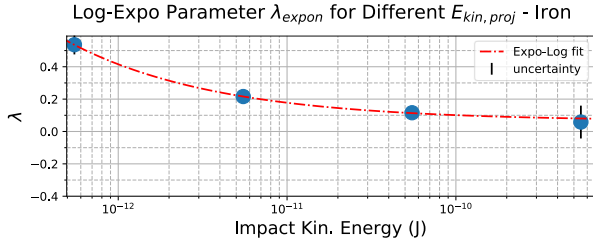


Figure 4. Distribution of λ_{expon} as a function of $E_{kin,imp}$ for Iron HVI data (blue) with a weighted log-exponential fit (red line).

3.3.2 Fragment Mass Distribution

PDF

The distribution of relative fragment mass $m_{frag}/m_{frag,tot}$ is shown in Fig. 6 for impact events in

which 2, 3, 4 and 5 fragments have been detected only (blue bars). For the PDF, a Weibull distribution as in Eq. 4 has been selected (red dotted line).

$$f(x, \lambda_{weibull}, k_{weibull}) = \frac{k_{weibull}}{\lambda_{weibull}} \left(\frac{x}{\lambda_{weibull}}\right)^{k_{weibull}-1} \cdot e^{-\left(\frac{x}{\lambda_{weibull}}\right)^{k_{weibull}}} \quad (4)$$

PDF Parameters

The resulting distribution of the Weibull parameters $\lambda_{weibull}$ as a function of N_{frag} is shown in Fig. 7 with a weighted exponential regression (red dotted line). Additionally, the distribution of the Weibull parameters $k_{weibull}$ as a function of N_{frag} is shown in Fig. 8 with a weighted linear regression (red dotted line).

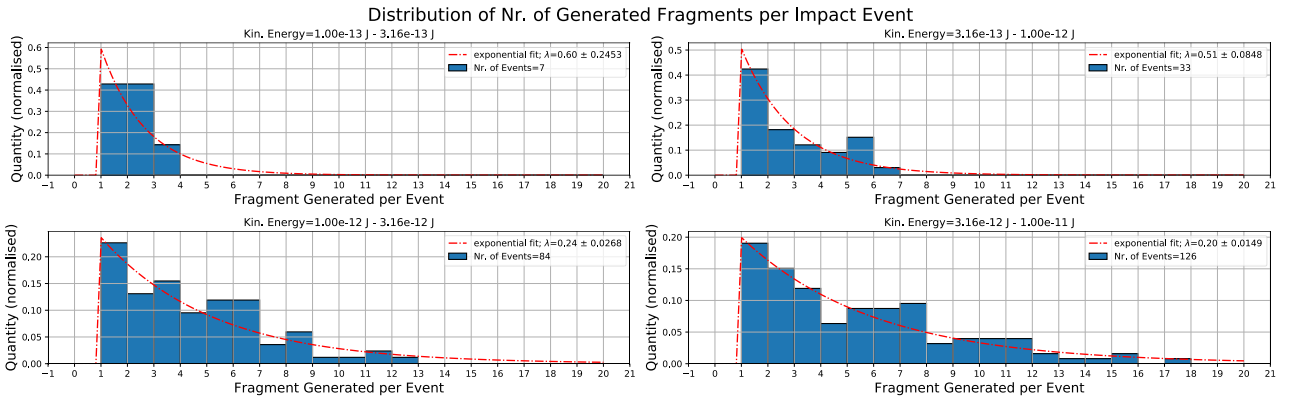


Figure 5. Distributions of N_{frag} for different kinetic impact energy $E_{kin,imp}$ bins. Blue: distribution of the Iron HVI data, red dotted line: Exponential PDF fit of the data.

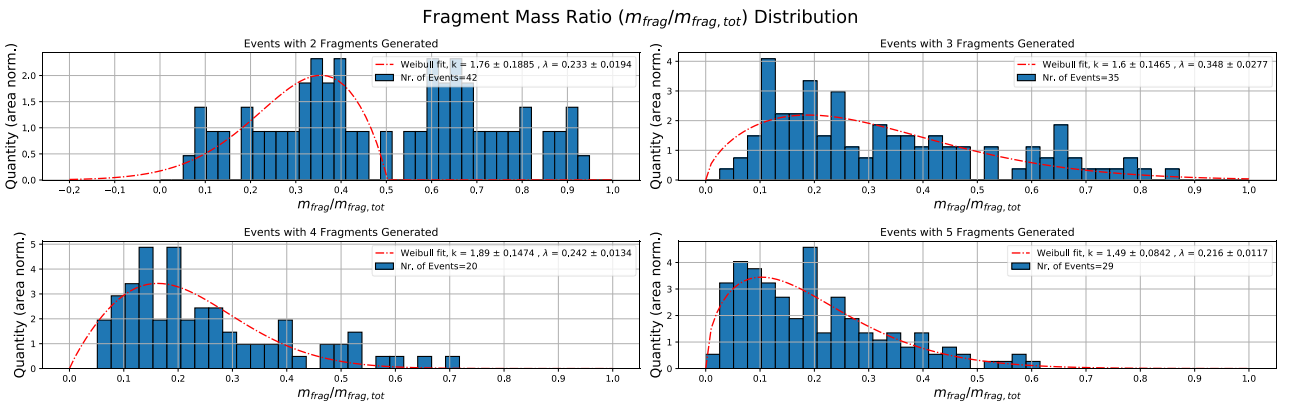


Figure 6. Distributions of $m_{frag}/m_{frag,tot}$ for impact events which generated 2, 3, 4, 5, 6 and 7 total fragments. Blue: distribution of the Iron HVI data, red dotted line: Weibull PDF fit of the data.

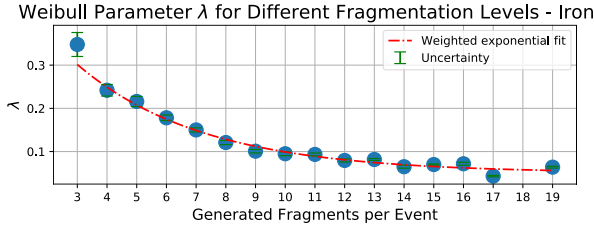


Figure 7. Distribution of $\lambda_{weibull}$ as a function of $N_{frag} > 2$ for Iron HVI data (blue) with a weighted exponential fit (red line).

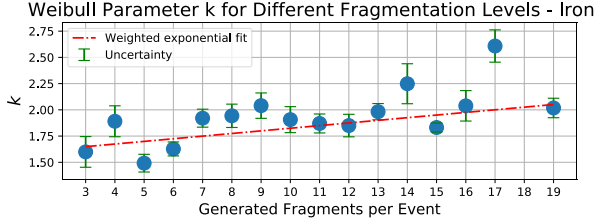


Figure 8. Distribution of $k_{weibull}$ as a function of $N_{frag} > 2$ for Iron HVI data (blue) with a weighted linear fit (red line).

As indicated by Fig. 6, for the case of only 2 fragments generated, a symmetrical distribution around $m_{frag}/m_{frag,tot} = 0.5$ can be observed. Consequently, the parameters $\lambda_{weibull}$ and $k_{weibull}$ are calculated as with respect to the number of generated fragments. In case of $N_{frag} = 2$, the values in Tab. 3 are applied for $\lambda_{weibull}$ and $k_{weibull}$.

Table 3. Parameters $\lambda_{weibull}$ and $k_{weibull}$ for $N_{frag} = 2$.

	$\lambda_{weibull}$	$k_{weibull}$
Brittle (Olivine)	0.234	1.68
Ductile (Iron)	0.233	1.76

In case of $N_{frag} > 2$, the coefficients a , b and c are applied as follows and in accordance with Tab. 4 and Tab. 5.

$$\lambda_{weibull}(N_{frag}) = a_{m1} \cdot e^{-b_{m1} \cdot N_{frag}} + c_m \quad (5)$$

$$k_{weibull}(N_{frag}) = a_{m2} \cdot N_{frag} + b_{m2} \quad (6)$$

Table 4. Coefficients for $\lambda_{weibull}$ for $N_{frag} > 2$.

Parameter	a_{m1}	b_{m1}	c_m
Brittle (Olivine)	1	0.42	0.084
Ductile (Iron)	0.51	0.23	0.05

Table 5. Coefficients for $k_{weibull}$ for $N_{frag} > 2$.

Parameter	a_{m2}	b_{m2}
Brittle (Olivine)	0.1	1.2
Ductile (Iron)	0.025	1.6

Total Fragment Mass

Due to uncertainty for fragment mass, a high range of $m_{frag,tot}/m_{proj}$ distribution was detected as illustrated in Fig. 9. Therefore, the most probable value of

$$m_{frag,tot}/m_{proj} = 0.95 \quad (7)$$

was assumed for the model, meaning that 95% of the projectile mass is converted to fragment mass. It is assumed that a small portion of the mass is converted to heat, absorbed by target and/or was not detected due to detector sensitivity.

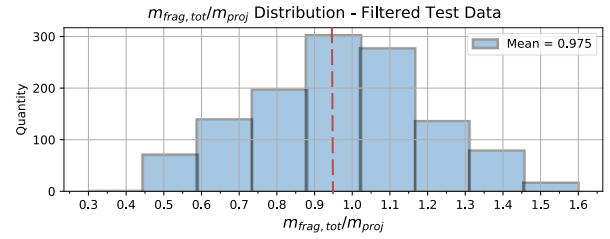


Figure 9. Distribution of $m_{frag,tot}/m_{proj}$ for Iron HVI data (blue) with highest peak at 0.95.

3.4 Density Distribution

It is assumed, that all the fragments are originated from the projectile and none from target. This assumption is also indicated by Smoothed Particle Hydrodynamics method (SPH) analysis done in prior to the HVI tests. Consequently, the following applies for all fragments:

$$\rho_{frag} = \rho_{proj} \quad (8)$$

Velocity Distribution

PDF

The relative velocity distribution V_{frag}/V_{proj} is shown in Fig. 12 for different $m_{frag}/m_{frag,tot}$ bins. Hereby, a Gaussian PDF has been selected for the distribution (red dotted line).

PDF Parameters

The resulting distribution of the Gaussian parameters μ_{gauss} as a function of $m_{frag}/m_{frag,tot}$ is shown in Fig. 10 with a weighted linear regression (red dotted line). Additionally, the distribution of the Weibull parameters σ_{gauss} as a function of $m_{frag}/m_{frag,tot}$ is shown in

Fig. 11 with a weighted linear regression (red dotted line).

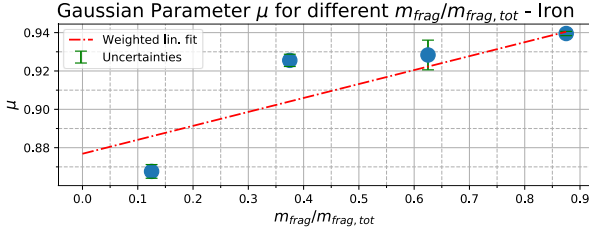


Figure 10. Distribution of μ_{gauss} as a function of $m_{frag}/m_{frag,tot}$ for Iron HVI data (blue) with a weighted linear fit (red line).

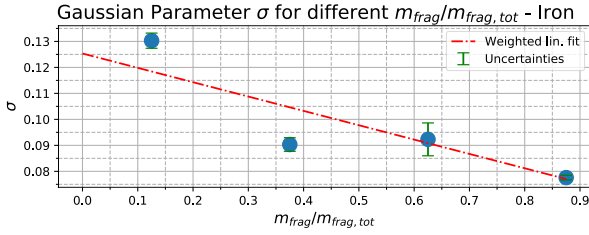


Figure 11. Distribution of σ_{gauss} as a function of $m_{frag}/m_{frag,tot}$ for Iron HVI data (blue) with a weighted linear fit (red line).

The parameters μ_{gauss} and σ_{gauss} are calculated as follows:

$$\mu_{gauss}(m_{frag}/m_{frag,tot}) = a_{v1} \cdot \frac{m_{frag}/m_{frag,tot}}{m_{frag}/m_{frag,tot} + b_{v1}} \quad (9)$$

$$\sigma_{gauss}(m_{frag}/m_{frag,tot}) = a_{v2} \cdot \frac{m_{frag}/m_{frag,tot}}{m_{frag}/m_{frag,tot} + b_{v2}} \quad (10)$$

with the parameters a and b taken from Tab. 6 and Tab. 7.

Table 6. Coefficients for μ_{gauss} .

Parameter	a_{v1}	b_{v1}
Brittle (Olivine)	-0.029	0.96
Ductile (Iron)	0.073	0.88

Table 7. Coefficients for σ_{gauss} .

Parameter	a_{v2}	b_{v2}
Brittle (Olivine)	-0.011	0.076
Ductile (Iron)	-0.055	0.13

3.5 Elevation Distribution

PDF

The relative elevation distributions $\theta_{frag}/\theta_{proj}$ is dependent for relative velocity of the fragments and the incident angle of the projectile. Consequently, the distribution of $\theta_{frag}/\theta_{proj}$ for different V_{frag}/V_{proj} bins. for $\theta_{proj} = 2^\circ$, $\theta_{proj} = 4^\circ$ and $\theta_{proj} = 6^\circ$ are shown in Fig. 13, 14 and 15 respectively. Hereby, a Weibull PDF (see Eq. 4) has been selected for the distribution (red dotted line).

As indicated by Fig. 13, particularly for the case of $\theta_{proj} = 2^\circ$, the low amount of available statistical data provides a challenge for deriving a sophisticated distribution. Consequently, the fragment elevation distribution of the model must be further refined and validated based on more statistical data obtained by further HVI tests.

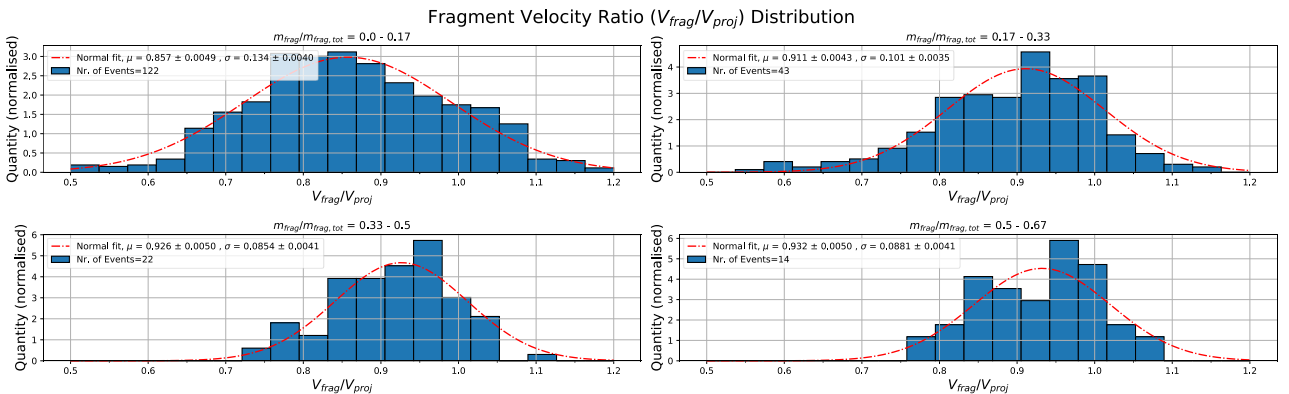


Figure 12. Distributions of V_{frag}/V_{proj} for different $m_{frag}/m_{frag,tot}$ bins. Blue: distribution of the Iron HVI data, red dotted line: Gaussian PDF fit of the data.

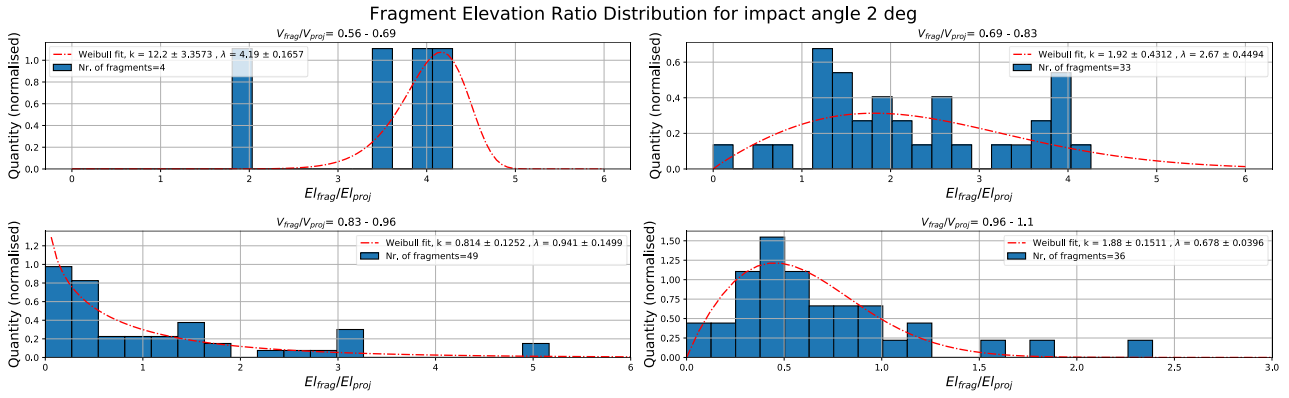


Figure 13. Distributions of $\theta_{frag}/\theta_{proj}$ for different V_{frag}/V_{proj} bins and $\theta_{proj} = 2^\circ$. Blue: distribution of the Iron HVI data, red dotted line: Weibull PDF fit of the data.

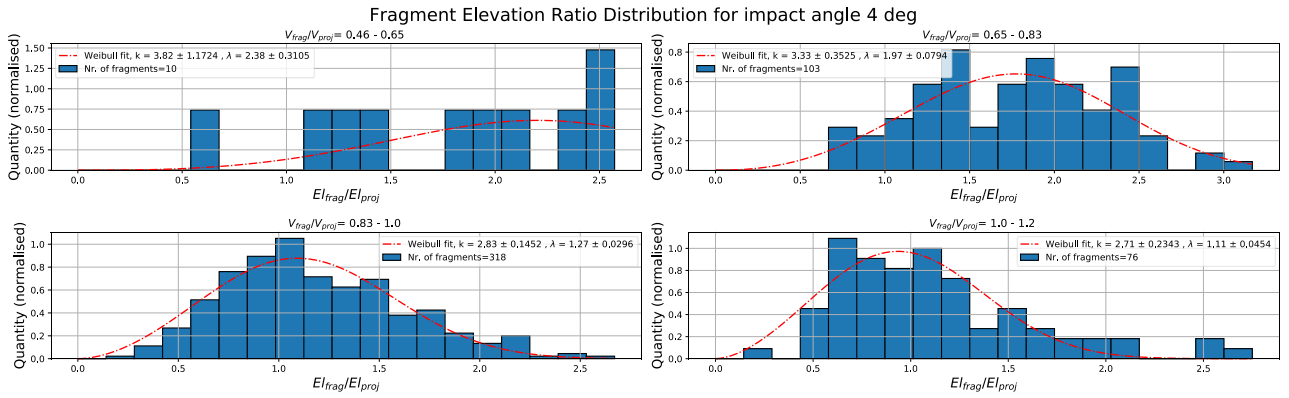


Figure 14. Distributions of $\theta_{frag}/\theta_{proj}$ for different V_{frag}/V_{proj} bins and $\theta_{proj} = 4^\circ$. Blue: distribution of the Iron HVI data, red dotted line: Weibull PDF fit of the data.

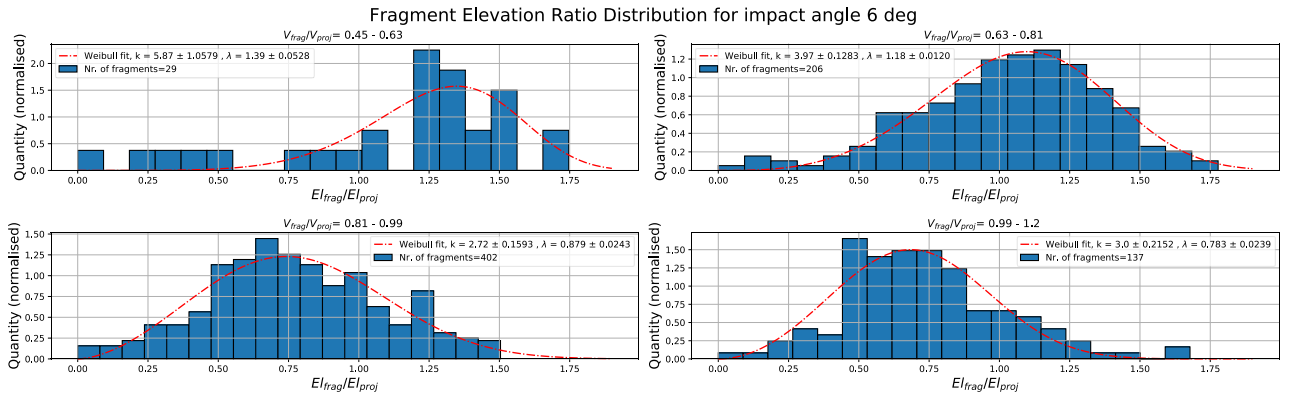


Figure 15. Distributions of $\theta_{frag}/\theta_{proj}$ for different V_{frag}/V_{proj} bins and $\theta_{proj} = 6^\circ$. Blue: distribution of the Iron HVI data, red dotted line: Weibull PDF fit of the data

PDF Parameters

Based on the available data, the resulting distribution of the Weibull parameters $k_{weibull}$ as a function of $m_{frag}/m_{frag,tot}$ is shown in Fig. 16 with a weighted linear regression (red dotted line). Additionally, the distribution of the Weibull parameters $\lambda_{weibull}$ as a

function of $m_{frag}/m_{frag,tot}$ is shown in Fig. 17 with a weighted linear regression (red dotted line). As indicated in Fig. 17, a different fragmentation characteristic can be observed for very shallow projectile incident angle (2°) compared to higher incident angle. Consequently, the critical impact angle of 2° was introduced for simulating the fragment elevation distribution.

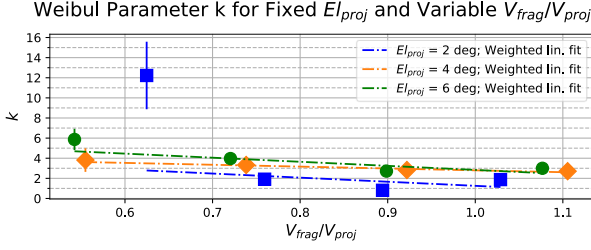


Figure 16. Distributions of $k_{weibull}$ as a function of $m_{frag}/m_{frag,tot}$ and impact incident angle for Iron HVI data (blue) with a weighted linear fit (red line).

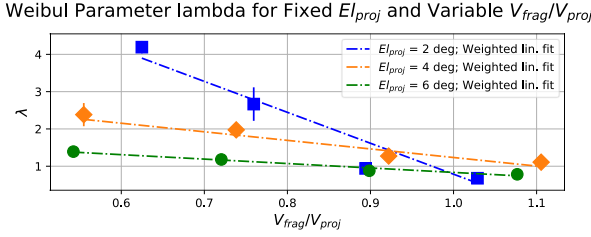


Figure 17. Distributions of $\lambda_{weibull}$ as a function of $m_{frag}/m_{frag,tot}$ and impact incident angle for Iron HVI data (blue) with a weighted linear fit (red line).

The Weibull PDF parameters $\lambda_{weibull}$ and $k_{weibull}$ are expressed as linear equations with two independent variables:

$$\lambda_{weibull}(\theta_{proj}, V_{frag}/V_{proj}) = a_{el1} + b_{el1} \cdot \theta_{proj} + c_{el1} \cdot V_{frag}/V_{proj} \quad (11)$$

$$k_{weibull}(\theta_{proj}, V_{frag}/V_{proj}) = a_{el2} + b_{el2} \cdot \theta_{proj} + c_{el2} \cdot V_{frag}/V_{proj} \quad (12)$$

The parameters a and b can be taken from Tab. 8 and Tab. 9 for the case $\theta_{proj} > 2$ and from Tab. 10 and Tab. 11 for the case $\theta_{proj} \leq 2$.

Table 8. Coefficients for $\lambda_{weibull}$ for $\theta_{proj} > 2$.

Parameter	a_{el1}	b_{el1}	c_{el1}
Brittle (Olivine)	1.44	-0.0986	0.37
Ductile (Iron)	3.75	-0.253	-1.45

Table 9. Coefficients for $k_{weibull}$ for $\theta_{proj} > 2$.

Parameter	a_{el2}	b_{el2}	c_{el2}
Brittle (Olivine)	-7.47	1.12	5.28
Ductile (Iron)	5.24	0.141	-3.11

Table 10. Coefficients for $\lambda_{weibull}$ for $\theta_{proj} \leq 2$.

Parameter	a_{el1}	b_{el1}	c_{el1}
Brittle (Olivine)	2.58	0	-1.59
Ductile (Iron)	9.08	0	-8.29

Table 11. Coefficients for $k_{weibull}$ for $\theta_{proj} \leq 2$.

Parameter	a_{el2}	b_{el2}	c_{el2}
Brittle (Olivine)	14.8	0	-13.7
Ductile (Iron)	5.33	0	-4.07

3.6 Azimuth Distribution

PDF

The fragment azimuth distribution is shown in Fig. 19 for impact events in which only 2, 3 and 4 fragments have been detected (blue bars). Hereby, a Gaussian PDF has been selected for the distribution (red dotted line). As can be seen, the expected value varies around 0° degree meaning that the majority of the fragments are oriented towards the downstream of the impact. This behaviour was also observed in SPH analysis done in prior to the HVI tests.

PDF Parameters

Based on the test data observation, the Gaussian parameters μ_{gauss} was defined as 0° for the model. The resulting distribution of the parameters σ_{gauss} as a function of N_{frag} is shown in Fig. 18 with a weighted root function regression (red dotted line).

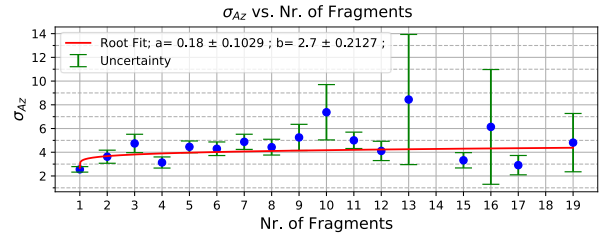


Figure 18. Distribution of σ_{gauss} as a function of N_{frag} for Iron HVI data (blue) with a weighted root function fit (red line).

Consequently, the parameters are calculated as follows:

$$\mu_{gauss} = 0^\circ \quad (13)$$

$$\sigma_{gauss} = (N_{frag} - 1)^{a_{az}} + b_{az} \quad (14)$$

with the parameters a and b listed in Tab. 12.

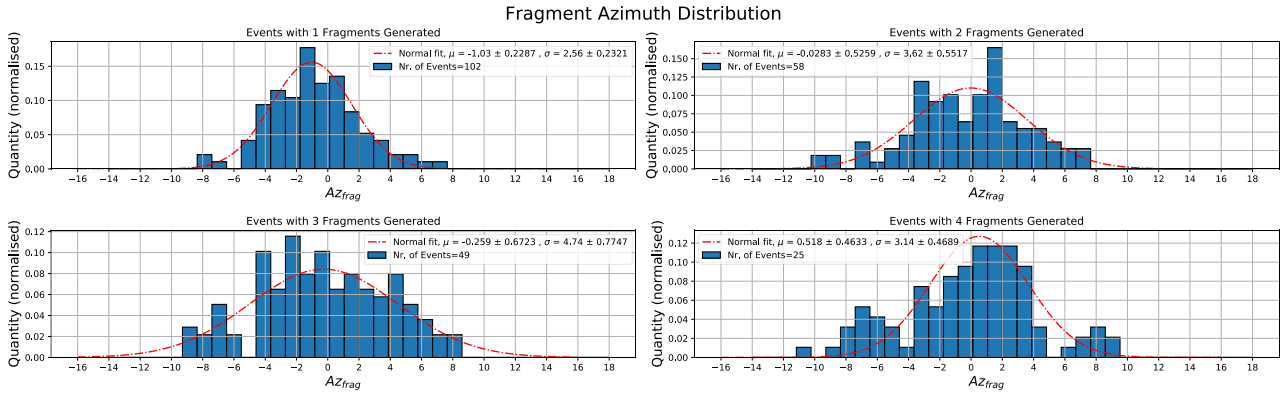


Figure 19. Distributions of fragment azimuth for impact events which generated 2, 3, 4, 5, 6 and 7 total fragments. Blue: distribution of the Iron HVI data, red dotted line: Gaussian PDF fit of the data.

Table 12. Coefficients for σ_{gauss} .

Parameter	a_{az}	b_{az}
Brittle (Olivine)	0.41	2.1
Ductile (Iron)	0.18	2.7

4 MODEL IMPLEMENTATION

GRIM is developed as a main FORTRAN routine with several subroutines/modules. Each fragment property is calculated in a dedicated module. As a result, the simulation of each fragment property can be easily modified, by exchanging the underlying subroutine in case of new findings in future HVI test campaigns. Therefore, based on the impacting projectile properties, GRIM is capable of predicting the number of generated fragments as well as their individual mass, velocity, density, elevation and azimuth angles. Moreover, a simulation seed can be provided as additional input to allow a deterministic random number generation. Tab. 13 provides an overview of the input and output parameters of GRIM.

The basic workflow of GRIM is illustrated in Fig. 20. The workflow was developed with respect to the observed data correlation as described in Fig. 3.

Table 13. Overview of model input and output parameters.

Parameter	Description	Unit
Input Parameters (Projectile)		
m_{proj}	Projectile Mass	kg
V_{proj}	Projectile Velocity	m/s
θ_{proj}	Projectile Elevation Angle	deg
ρ_{proj}	Projectile Density	kg/m ³
-	Simulation Seed	-
Output Parameters (Fragment)		
N_{frag}	Number of generated fragments per impact event	-
m_{frag}	Individual Fragment Masses	kg
V_{frag}	Individual Fragment Velocities	m/s
θ_{frag}	Individual Fragment Elevation Angles	deg
φ_{frag}	Individual Fragment Azimuth Angles	deg

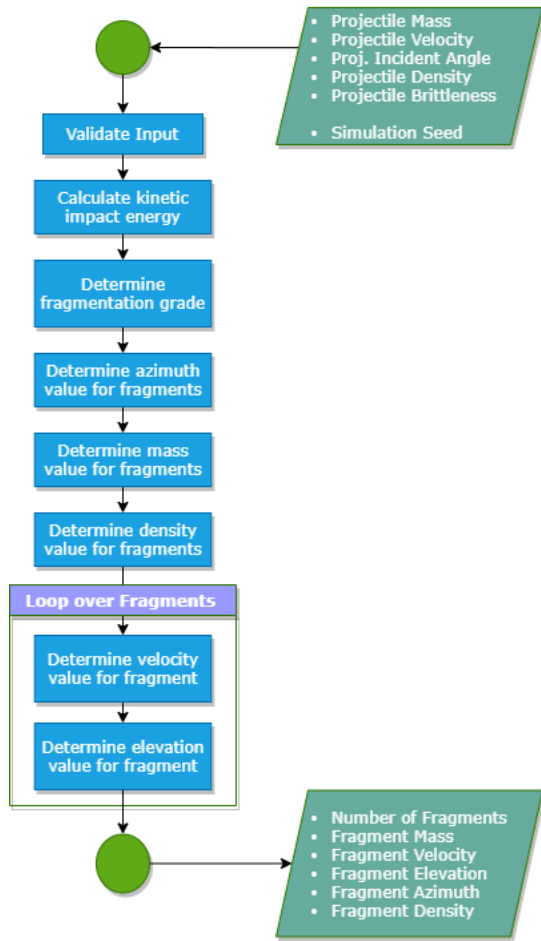


Figure 20. Simplified workflow of GRIM.

5 MODEL VERIFICATION AND VALIDATION

The model output was validated against the HVI test data. Initially, it was foreseen to split the HVI test data to a development set for the model development activity and a test set for model validation activity. However, due to the relative low number of available data for statistical analysis, the decision was made to use the entirety of the available data for the model development to increase the statistical quality. However, this leads to the loss of an independent test data. Consequently, the model has to be further validated against additional HVI data gained in a planned second HVI test campaign. The model was validated based on two approaches: Module-wise and system-wise.

5.1 Module Verification and Validation

Each module (e.g. azimuth distribution, velocity distribution etc.) was validated separately based on the HVI test data. Hereby, the input for the module was extracted from the database and the resulting output/predicted value for the fragment property was compared to the detected value in the HVI data. As a

result, the *Prediction Accuracy* parameter was introduced as described in Eq. 15. Due to the application of random number generators, the mean value after 1000 Monte Carlo iterations was used as a representative of the predicted value.

$$Prediction\ Accuracy = \frac{(Mean\ Predicted\ Value)_{MC}}{Detected\ Value} \quad (15)$$

Consequently, a prediction accuracy of “1.0” would mean that the average value predicted by the model after several Monte Carlo iterations equals to the detected value in the HVI data while a value below or above “1.0” would mean that the model has provided an underrated or overrated prediction respectively. In general, the validation of all the modules have shown a good compliance to the detected HVI test values. For instance, Fig. 21 shows the distribution of the mean prediction accuracy for fragment relative velocity achieved after 1000 Monte Carlo iterations $(\tilde{v}_{frag}/v_{proj})_{MC,pred}$ over all of the impact events. The distribution is also expressed in form of a Gaussian distribution. As can be seen, for the majority of the impact events, the model has achieved a prediction accuracy near “1.0”. The mean prediction accuracies for fragment relative mass $(\tilde{m}_{frag}/m_{proj})_{MC,pred}$, fragment relative elevation $(\tilde{\theta}_{frag}/\theta_{proj})_{MC,pred}$ and number of generated fragments $(\tilde{N}_{frag})_{MC,pred}$ gained for all of the impact events are displayed in Fig. 22, 23 and 24. As demonstrated in Fig. 24, the model slightly underrated the number of generated fragments in an impact. This behaviour will be further analysed in the second test campaign.

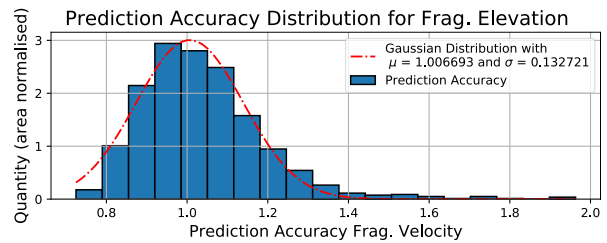


Figure 21. Distribution of prediction accuracy $(\tilde{v}_{frag}/v_{proj})_{MC,pred}$ over all impact events achieved after 1000 Monte Carlo iterations.

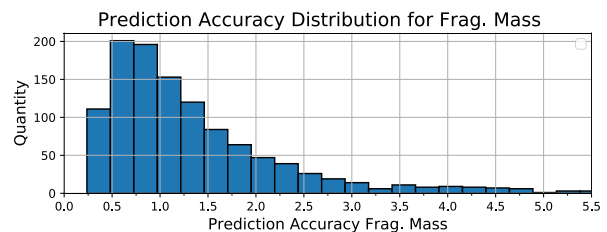


Figure 22. Distribution of prediction accuracy $(\tilde{m}_{frag}/m_{proj})_{MC,pred}$ over all impact events achieved after 1000 Monte Carlo iterations.

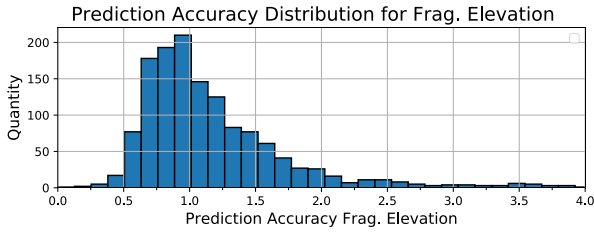


Figure 23. Distribution of prediction accuracy $(\tilde{\theta}_{frag}/\theta_{proj})_{MC, pred}$ over all impact events achieved after 1000 Monte Carlo iterations.

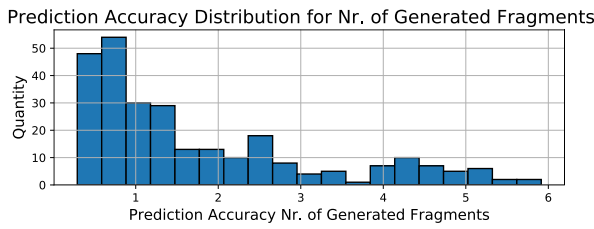


Figure 24. Distribution of prediction accuracy $(\tilde{N}_{frag})_{MC, pred}$ over all impact events achieved after 1000 Monte Carlo iterations.

5.2 System Verification and Validation

A system verification was performed to verify the generic workflow concept of GRIM (see Fig. 20) and the inclusion of all of the modules into this process. This was done by providing the impact properties of all the impact events in the HVI test data to the main GRIM routine and comparing the predicted to the detected fragment distributions. Due to the workflow, GRIM determines the number of generated fragments based on the impact condition. The fragment quantity will then serve as input to other fragment property modules and thus influence the output of the model significantly. Therefore, the parameter *Prediction Accuracy* as a mean to perform a 1-to-1 comparison of fragment property prediction is not possible due to different numbers of generated fragments.

Consequently, the predicted vs detected distributions have been compared with each other as presented in Fig. 25, 26, 27, 28 and 29. In Fig. 26, the peak at $m_{frag}/m_{frag, tot} = 1$ represents those projectiles that have experienced no fragmentation and thus the resulting fragment mass being the same as the projectile mass. As can be seen, the model shows a good prediction compliance to the detected HVI test data. A more elaborated system validation is foreseen after the second test campaign.

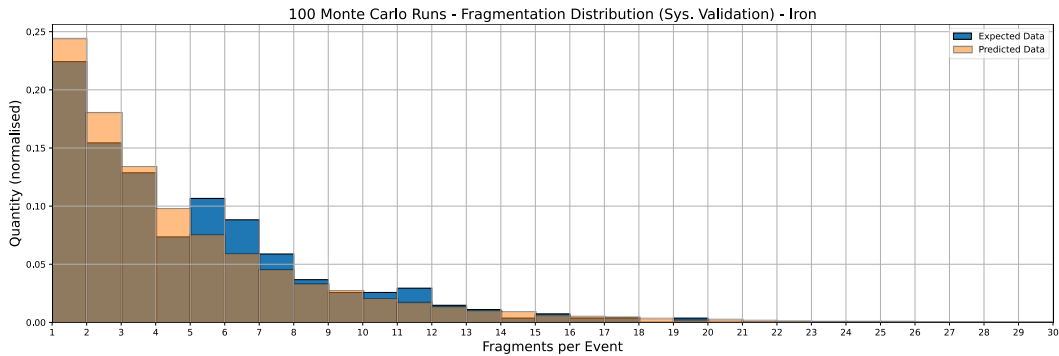


Figure 25. Area normalized distribution of predicted and detected N_{frag} (generated fragments per event) on system level after 100 Monte Carlo iterations. Blue: Detected data from Iron HVI test. Orange: Predicted data via GRIM.

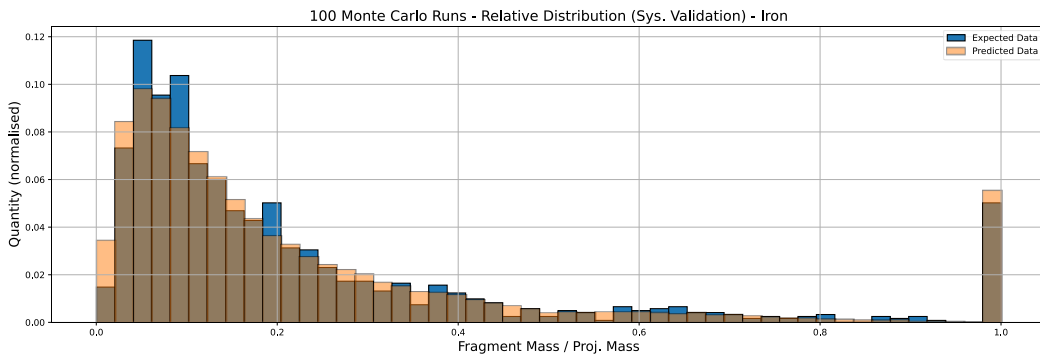


Figure 26. Area normalized distribution of predicted and detected $m_{frag}/m_{frag, tot}$ on system level after 100 Monte Carlo iterations. Blue: Detected data from Iron HVI test. Orange: Predicted data via GRIM.

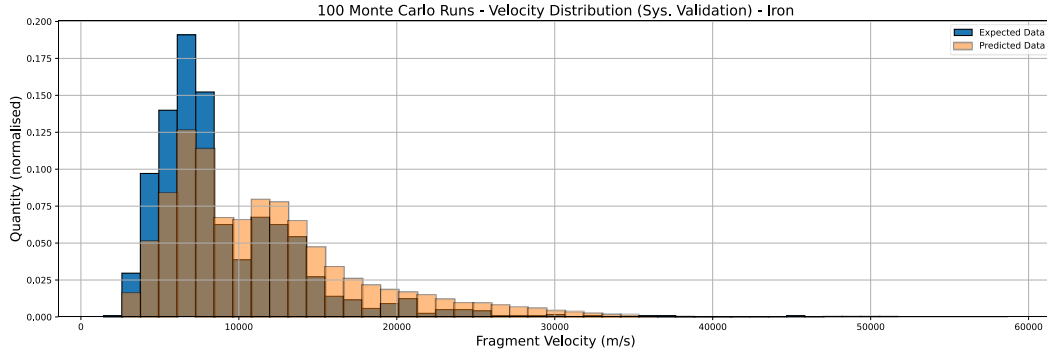


Figure 27. Area normalized distribution of predicted and detected V_{frag} on system level after 100 Monte Carlo iterations. Blue: Detected data from Iron HVI test. Orange: Predicted data via GRIM.

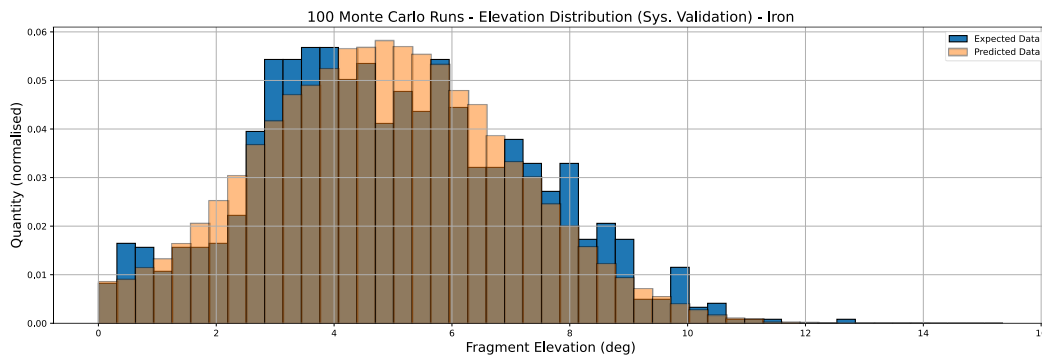


Figure 28. Area normalized distribution of predicted and detected θ_{frag} on system level after 100 Monte Carlo iterations. Blue: Detected data from Iron HVI test. Orange: Predicted data via GRIM.

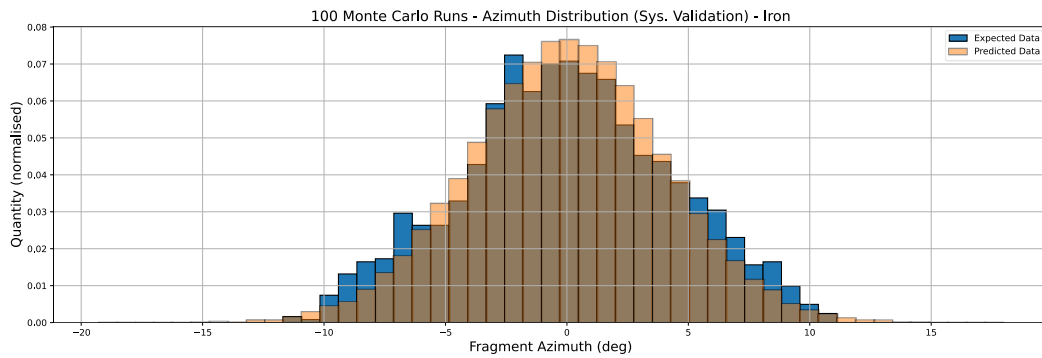


Figure 29. Area normalized distribution of predicted and detected θ_{frag} on system level after 100 Monte Carlo iterations. Blue: Detected data from Iron HVI test. Orange: Predicted data via GRIM.

6 APPLICATION DEMONSTRATION

To demonstrate the application capabilities of the model for analysing and tracking focused cascading effects inside X-ray optic tubes, the model was implemented into ESA’s MMOD risk assessment tool “ESABASE2/Debris” as a prototype. Hereby, the geometry handling and raytracing features of ESABASE2 were utilised to initialise a single grazing

projectile impact inside a tube (representing a silicon-pore in X-ray detectors), predict the resulting fragments, trace fragment secondary impacts inside the tube and repeat the cycle upon further impact detection until the fragments have reached the back wall of the tube representing a CCD camera location. The projectile parameters are listed in Tab. 14. Furthermore, the dimensions of the modelled rectangular tube are: 65 mm x 0.83 mm x 0.606 mm (LxWxH). As shown in Fig. 30,

with applying GRIM, the fragmentation cascading process of a projectile entering the tube can be simulated resulting in hundreds of fragments focused on the tube's back wall. The implementation into ESABASE2 could be extended in the future to also allow to derive statistics about the properties of the fragments reaching the backwall.

Table 14. Projectile parameters for simulation.

Proj. Parameter	Value
Mass	5e-15 kg
Diameter	1.07e-6 m
Velocity	13.02 km/s
Density	7800 kg/m ³
Elevation	2.86°
Type	Ductile

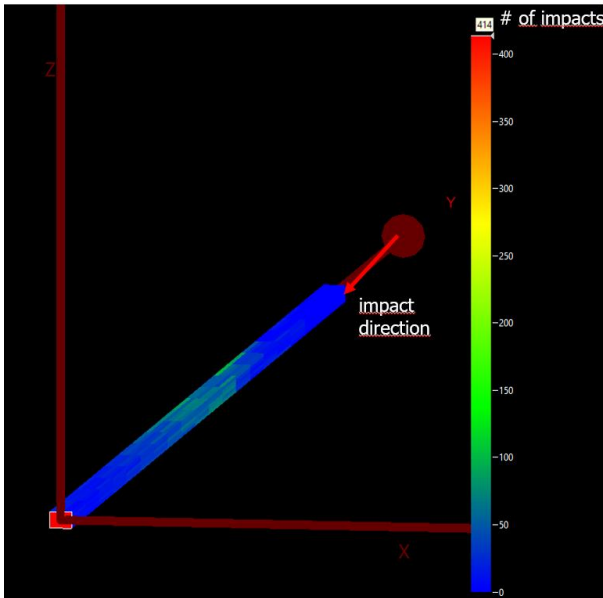


Figure 30. Demonstration of GRIM's focused cascading analysis capabilities using the tool ESABASE2/Debris.

7 SUMMARY AND CONCLUSION

A new statistical model was developed to predict the resulting fragment properties based on the projectile properties for very shallow impact angles on mirror surfaces. The model was developed based on fragment data gained from a series of dedicated HVI tests. Based on provided projectile parameters (mass, velocity, density and incident angle) the model predicts the number of generated fragments and their properties (mass, velocity, density, elevation and azimuth angles). Hereby, the model can distinguish between ductile and

brittle projectiles. The model was validated against the HVI test data and shows a good compliance for the predictions.

Consequently, by implementing into sophisticated MMOD risk assessment tools, the model allows to analyse focused cascading effects of particles inside X-ray telescope by using the 3D model of the instrument. This was demonstrated by implementing the model into ESA's ESABASE2/Debris tool and perform a cascading simulation based on a simple tube geometry.

In contrast to Smoothed Particle Hydrodynamics methods, the statistical model provides the advantage of performing impact simulations in a fraction of the required time and computational power. Thus, it enables the simulation of cascading impact events inside complex mirror systems in a reasonable time frame.

A second HVI test campaign is foreseen, to gain additional reference data for further model refinement and validation purpose. Furthermore, the model will be extended to allow the assessment of mirror surface cratering due to grazing impacts.

8 REFERENCE

1. Meidinger, N., et al. (2003) "Experimental Verification of a Micrometeoroid Damage in the PN-CCD Camera System aboard XMM-Newton", Proceedings of SPIE – the International Society for Optical Engineering, 4851, 243-254; doi:10.1117/12.461154
2. Y.W.Li, A. Mocker, R. Srama (2020). „Test Campaign 1 and Test Analysis 1, Technical Note 5/6”, 4000170405/17/NL/LF